Supplementary Information

Pyridinic-N exclusively enriched CNT encapsulated NiFe interfacial alloy nanoparticles on knitted carbon fiber cloth as bifunctional oxygen catalysts for biaxially flexible zinc-air batteries

Milan Babu Poudel[a,b], Subramanian Vijayapradeep[a], Karthikeyan Sekar[c], Jong Seok Kim[d], Dong Jin Yoo[a,b,*]

[a]Department of Energy Storage/Conversion Engineering (BK21 FOUR) of Graduate School, Hydrogen and Fuel Cell Research Center, Jeonbuk National University, 567 Baekje-daero, Deokjin-gu, Jeonju-si, Jeollabuk-do, 54896, Republic of Korea

[b]Department of Life Science, Jeonbuk National University, 567 Baekje-daero, Deokjin-gu, Jeonju-si, Jeollabuk-do, 54896, Republic of Korea

[c]Department of Chemistry, Faculty of Engineering and Technology, SRM institute of Science and Technology, Kattankulathur, Tamil Nadu 603 203, India

[d]School of Semiconductor and Chemical Engineering, Jeonbuk National University, 567 Baekje-daero, Deokjin-gu, Jeonju-si, Jeollabuk-do, 54896, Republic of Korea

*Corresponding authors, Email ID: djyoo@jbnu.ac.kr; (Prof. Dong Jin Yoo),
Fax: +82-(0) 63-270-3909 Tel: +82-(0) 63-270- 3608

Materials

Iron (II) nitrate nonahydrate ($Fe(NO_3)_3.9H_2O$, Sigma-Aldrich, USA, >98 %), nickel nitrate hexahydrate ($Ni(NO_3)_2.6H_2O$, Sigma-Aldrich, USA, >99.9 %), 2-aminoterapthalic acid ($H_2NC_6H_3$-1,4-$(CO_2H)_2$, , Sigma-Aldrich >99 %), ammonium fluoride (NH_4F, Sigma-Aldrich , USA, >98.0 %). Urea ($(NH_2)CO$, Alfa-Aesar, USA, >990 %), Potassium hydroxide (KOH, Samchun, Korea, 95.0%) and Ethanol (Samchun, Korea, 99.9%) were directly used without processing. DI water was used throughout the experimental work. Zinc foil (0.25 mm) was obtained from Alfa Aesar, UK). The knitted carbon fiber cloth was immersed in 6 M HNO_3 at 60^oC for and subsequently rinsed with water for several times to remove impurities.

Physicochemical characterizations

The surface morphologies and micro/nanostructures were analyzed by field emission scanning electron microscopy (FESEM) with energy dispersive spectroscopy (EDS) (FESEM, S-7000, Hitachi, Japan) and transmission electron microscopy (TEM, JEM-2200, 200 kV, JEOL, Japan) (Center for University-wide Research Foundation, (CURF), Jeonbuk National University). The crystallographic properties of the samples were evaluated by powder X-ray diffraction (XRD, Rigaku, Cu Kα λ = 1.540 Ao, 30 kV, 40 mA) and X-ray photoelectron spectroscopy (XPS, ESCLAB 250, USA, Korea Basic Science Institute, Jeonju). Further, X-ray absorption spectroscopy (BL15, Kyushu Synchrotron Light Research Center (SAGA-LS; Tosu, JAPAN) in transmission mode) was used to investigate the chemical compositions and oxidation states of the catalysts.

Electrochemical measurements

For OER

Electrocatalytic performance tests were performed with three electrodes configuration using Gamry instrument Reference 600 (potentiostat/Galvanostat/ZRA) in 1 M KOH. The device comprised of reference electrode (Ag/AgCl), counter electrode (Pt wire) and our prepared samples used as working electrode (Figure S1). All the active materials were directly used as binder free electrode. Since the potentials of the working electrodes are measured with reference to the Ag/AgCl electrode, the resulting potentials are converted to reversible hydrogen electrode (RHE) with the following Nernst equation [SR1]:

$$E\ vs\ RHE = E_{Ag/AgCl} + 0.0596pH + E^{o}_{Ag/AgCl}$$

Where, $E^{o}_{Ag/AgCl}$ =0.1976 at 25 ^{o}C

Before the OER activity test, cyclic voltammetry was performed at 25 mV s^{-1} for 30 cycles. After stabilization, linear sweep voltammetry (LSV) was performed at 1 mV s^{-1} within potential range of 0 to 1.2 V. Electric double layer test: for OER reaction, cyclic voltammetry was executed at various scan rates. Electrochemical impedance spectroscopy (EIS) was measured with frequency range of 0.01 to 10^6 Hz. Chronopotentiometry was used to evaluate the stabilities of electrocatalyst. A commercial electrocatalyst. RuO_2 was cast on the knitted carbon cloth and its OER activity was also compared to our prepared electrocatalysts. All the potential values are corrected according to the following equation.

$$E_{corrected} = E - iR_s$$

Here, E is experimentally determined potential, *i* is current density and R_s is equivalent series resistance.

Calculation of electrochemically active surface area (ECSA)

The electrochemically active surface area (ECSA) of the prepared catalyst was investigated through calculating the double-layer capacitance (Cdl) by recording the CV curve with the non-Faradic region with different scan rate of 10-50 mV s^{-1}. The slope of capacitive current (Δj = j anode – j cathode) vs scan rate was double the value of Cdl. The double-layer capacitance (Cdl) is directly proportional to ECSA, as given below:

$$ESCA = \frac{C_{dl}}{C_d}$$

ECSA = Electrochemical active surface area (ECSA),

Cdl = Double layer capacitance

Cs = Specific capacitance (0.040 mF cm^{-2}).

For ORR

For ORR test, NiFe-N-CNT was scrapped out from the KCC. 2.5 mg of the NiFe-N-CNT and 30 µL of Nafion solution was dispersed in 1 mL of ethanol and DI water (1:1) solution sonicated for 15 min to generate homogenous solution. The catalyst's ink (approximately 20 µL) was drop-casted on the surface of rotating disc electrode (5 mm diameter) and dried at 50 ^oC for few hours. All the ORR activities were performed using Pt-wire as counter electrode, Ag/AgCl reference electrode and prepared RRD as working electrode.

The ORR performance of the as prepared sampleas was investigated by cyclic voltammetry (CV) in N_2 and O_2 saturated 0.1 M KOH at room temperature at 20 mV s^{-1}. Linear sweep voltammetry were conducted under contineous O_2 discharge at 10 mV s^{-1} at various rotation speed (400-2800 rpm). Long term stability was performed by chronoamperometry at a constant 1600 rpm under contineous supply of O_2 gas under a constant potential of -0.3 V Vs Ag/AgCl.

Calculationof number of electron transfer during ORR

Koutechy-Levich (K-L) plots were used to determine the number of electron transferred at various potentials. (J^{-1} vs $\omega^{-1/2}$)

$$\frac{1}{J} = \frac{1}{J_L} + \frac{1}{J_K} = \frac{1}{B\omega^{1/2}} + \frac{1}{J_K}$$

$$B = 0.62\, nFC_0 D_0^{2/3} v^{-1/6}$$

Where, J, J_L, and J_K are measured current density, difussion-limiting current density and kinetic limiting current density, rerspectively. Kinetic current density ($J_K = \frac{J_{lim} \times j}{J_{lim} - j}$) [1]

F= Faradays constant (F = 96485 C mol^{-1})

ω = angular velocity for RDE (rad s^{-1})

D_o = oxygen diffusion coeffecient (1.9×10^{-5} $cm^{-2}S^{-1}$)

C_o = Satureted oxygen concentration of 1.2×10^{-3} mol L^{-1}

N = number of electron transfer during ORR

V = kinetic velocity of electrolyte (0.01 cm^2 s^{-1})

From KL plot, the electron transfer number of the NiFe-N-CNT-KCC catalysts during ORR was ~3.93, approaching that of the commercial Pt/C catalyst, satisfying desired $4e^-$ reduction pathways. The general $4e^-$ oxidation pathway for the OER in alkaline media is the reverse of the ORR shown below [2]:

$$M + OH^- \rightarrow MOH + e^-$$

$$MOH + OH^- \rightarrow MO + H_2O + e^-$$

$$MO + OH^- \rightarrow MOOH + e^-$$

$$MOOH + OH^- \rightarrow MOO^- + H_2O + O_2 + e^-$$

$$MOO^- + e^- \rightarrow M + OOH + O_2 + e^-$$

Calculation of TOF for OER

The oxygen TOF per site of the NiFe-N-CNT-KCC catalyst was calculated using the following formula (S4):

$$\#\, O_2 = \frac{\#\ total\ oxygen\ turnovers/cm^2\ \ geometric\ area}{\#\ active\ sites/cm^2\ \ geometric\ area}$$

The total number of oxygens turn overs were calculated from the current density according to

$$\#\, O_2 = \left(j\frac{mA}{cm^2}\right)\left(\frac{\frac{1C}{s}}{1000\ mA}\right)\left(\frac{1mol\ e^-}{96485\ C}\right)\left(\frac{1mol\ O_2}{4\ mol\ e^-}\right)\left(\frac{6.02\times10^{23}mol\ O_2}{1mol\ O_2}\right)1.56_{\times}10^{15}\frac{\frac{O_2}{s}}{cm^2}per\ \frac{mA}{cm^2}$$

Further, Ni and Fe content of NiFe-N-CNT-KCC catalyst was quantified by using ICP-OES analysis was about ~14 wt. and 27 wt. Accordingly, the density of active sites based on the Ni and Fe is:

$$\left(\frac{14}{58.693}+\frac{27}{55.845}\right)\times\frac{1mmol}{100\,mg}\times 3\frac{mg}{cm^2}\times 6.022\times 10^{20}\,\frac{sites}{mmol}=12.93\times 10^{18} sites\ cm^{-2}$$

For example, TOF of the catalyst at an overpotential of 380 mV was calculated as follows,

$$TOF=\frac{394.78\times 1.61\times\ 10^{15}\frac{O_2/s}{cm^2}}{12.93\times 10^{18}\ sites\ cm^{-2}}=0.049\ s^{-1}$$

For Zinc air battery

The optimized NiFe-N-CNT-KCC active materials were directly used as binder free air cathode and Zn foil (0.25 mm) was used to fabricate Zn-air battery. 6 M KOH mixed with 0.2 M $Zn(CH_3CO)_2$ was used as electrolyte. Long term charge-discharge cycling stability test were performed in Gamry 600 electrochemical workstation. The power density (mW cm^{-2}) and specific capacity (mA h g^{-1}) for NiFe-N-CNT-KCC based Zn-air battery were determined by polarization curve using following relation:

$$power\ density\ (mW\ cm^{-2}) = Voltage\ \times current$$

$$Specific\ capacity\ (mA\ h\ g^{-1}) = \frac{current\ \times service\ hours}{mass\ of\ Zn\ consumed}$$

For flexiable Zn air battery

We fabricated solid state flexible Zn air battery using optimized NiFe-N-CNT-KCC as air cathode and Zn foil as anode sandwiching gel electrolyte within it. A gel electrolyte was prepared with 0.2 M $Zn(CH_3CO)_2$ containing PVA-KOH.

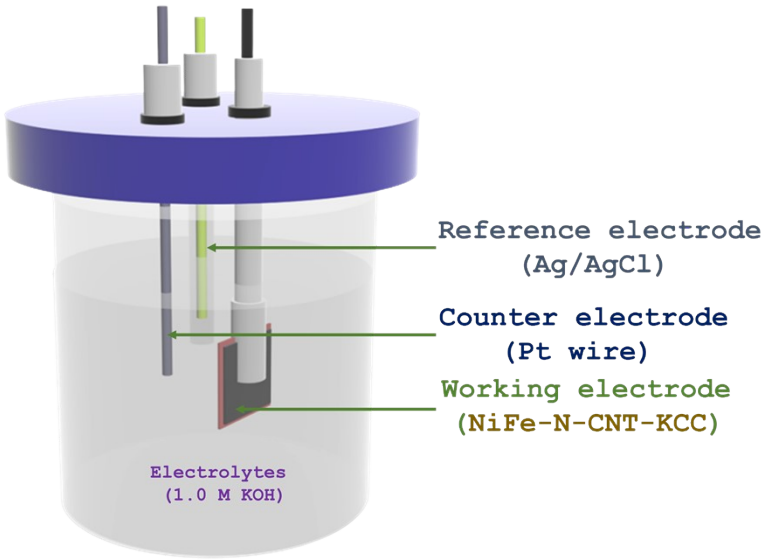

135

136 Figure S1. OER experimental setup for three electrode cell configurations, indicating reference

137 electrode, counter electrode and working electrode.

138

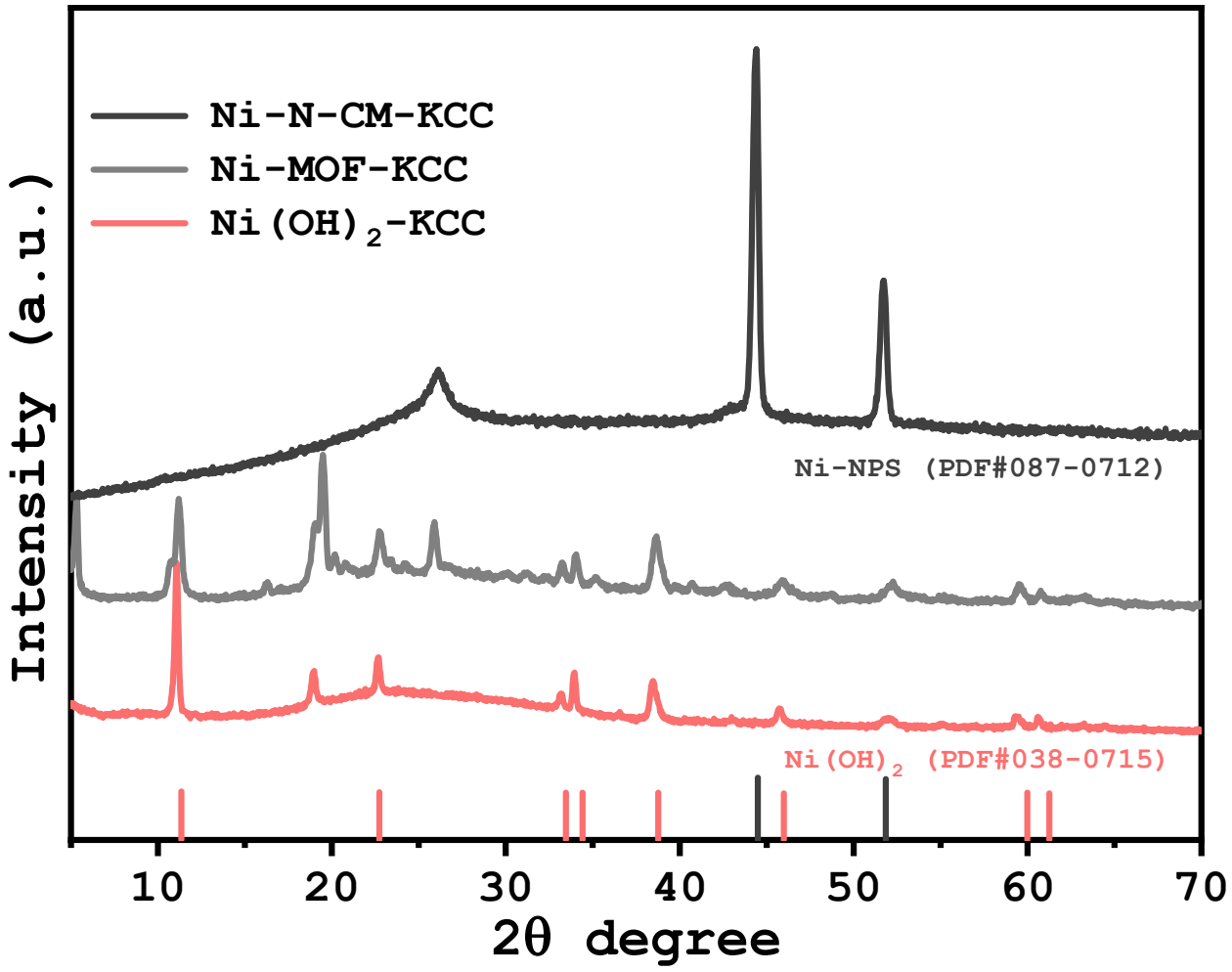

139

140 Figure **S2**: XRD patterns of Ni-N-CM-KCC and its precursor.

141

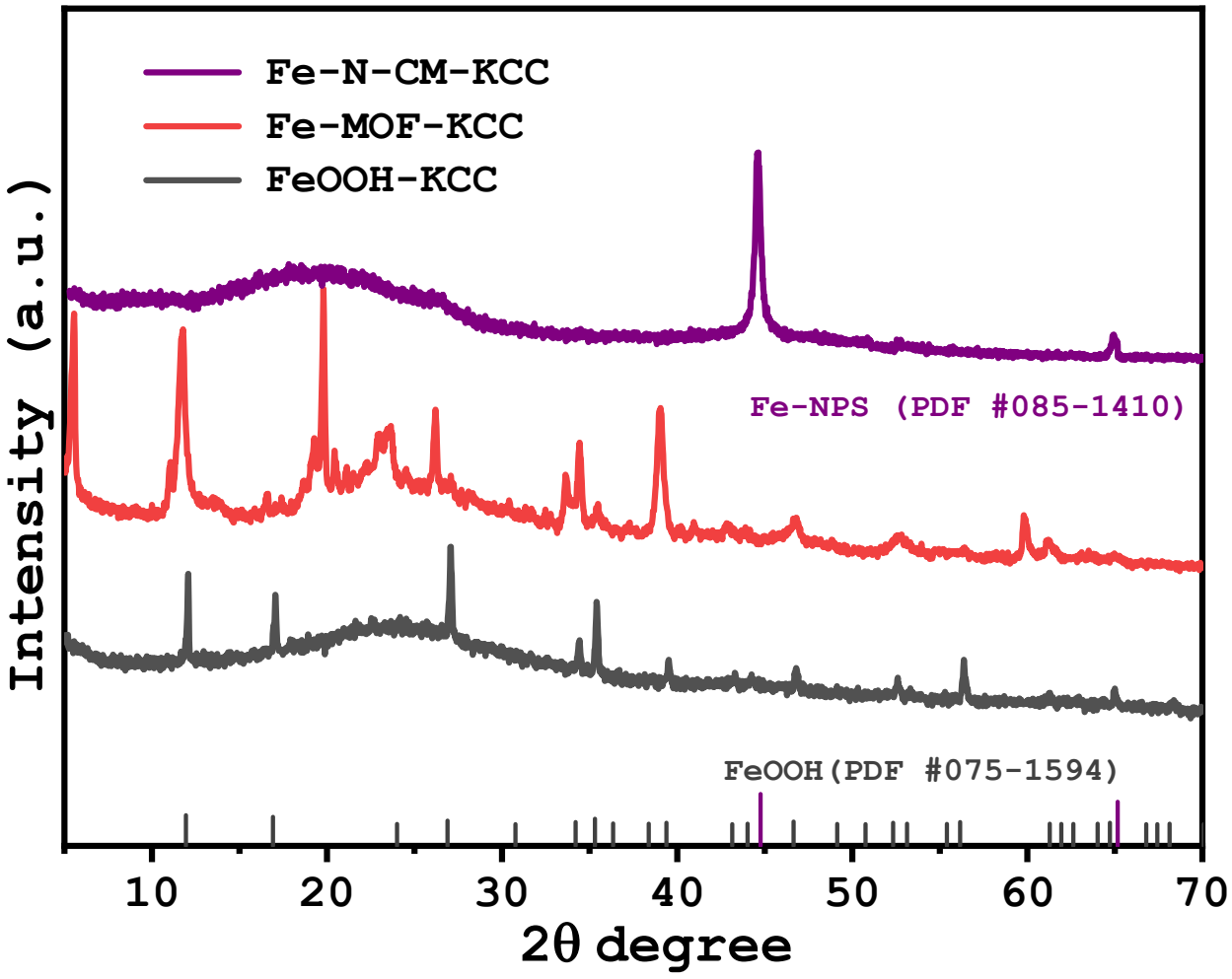

142

143 Figure **S3**: XRD patterns of Fe-N-CM-KCC and its precursor.

144

145

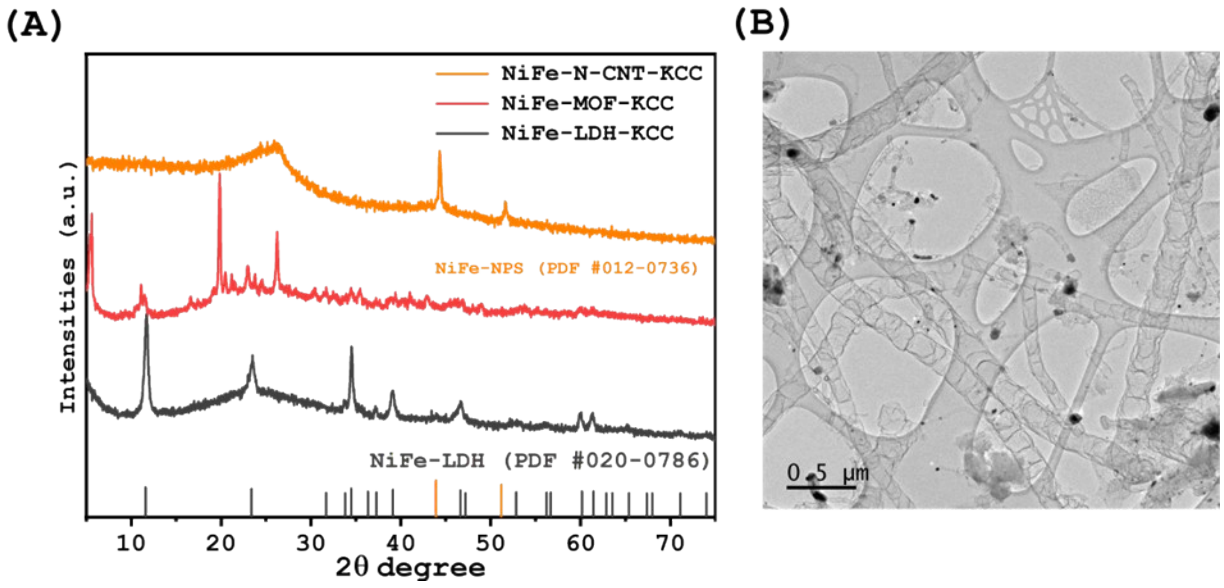

146

147 Figure **S4**: XRD patterns of NiFe-N-CNT-KCC and its precursor, and TEM image of NiFe-N-

148 CNT-KCC

149

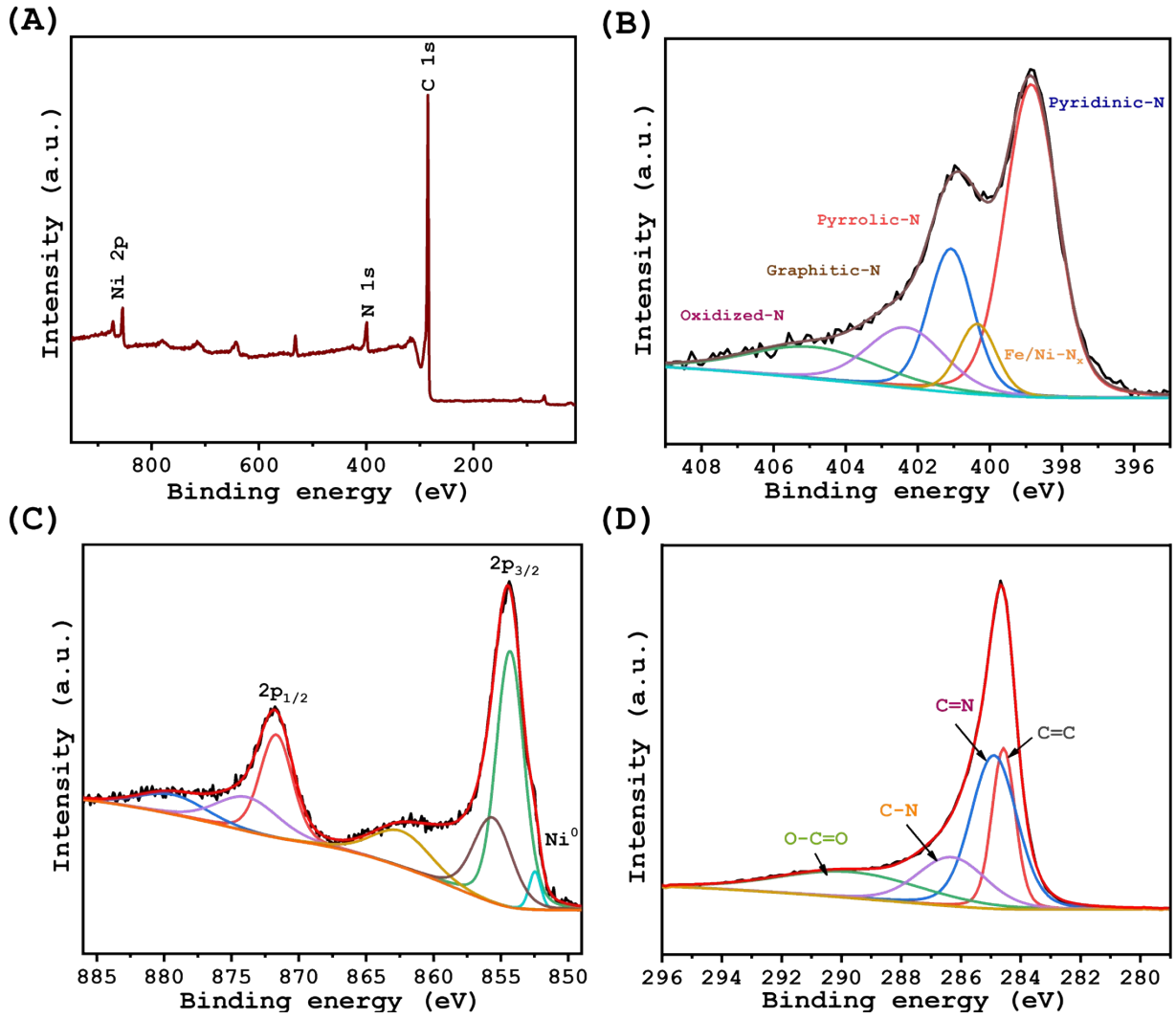

150

151 Figure **S5**. XPS studies for Ni-N-CM-CC, (A) survey spectrum, (B) N 1s, (C) Ni 2p, and (D) C

152 1s.

153

154

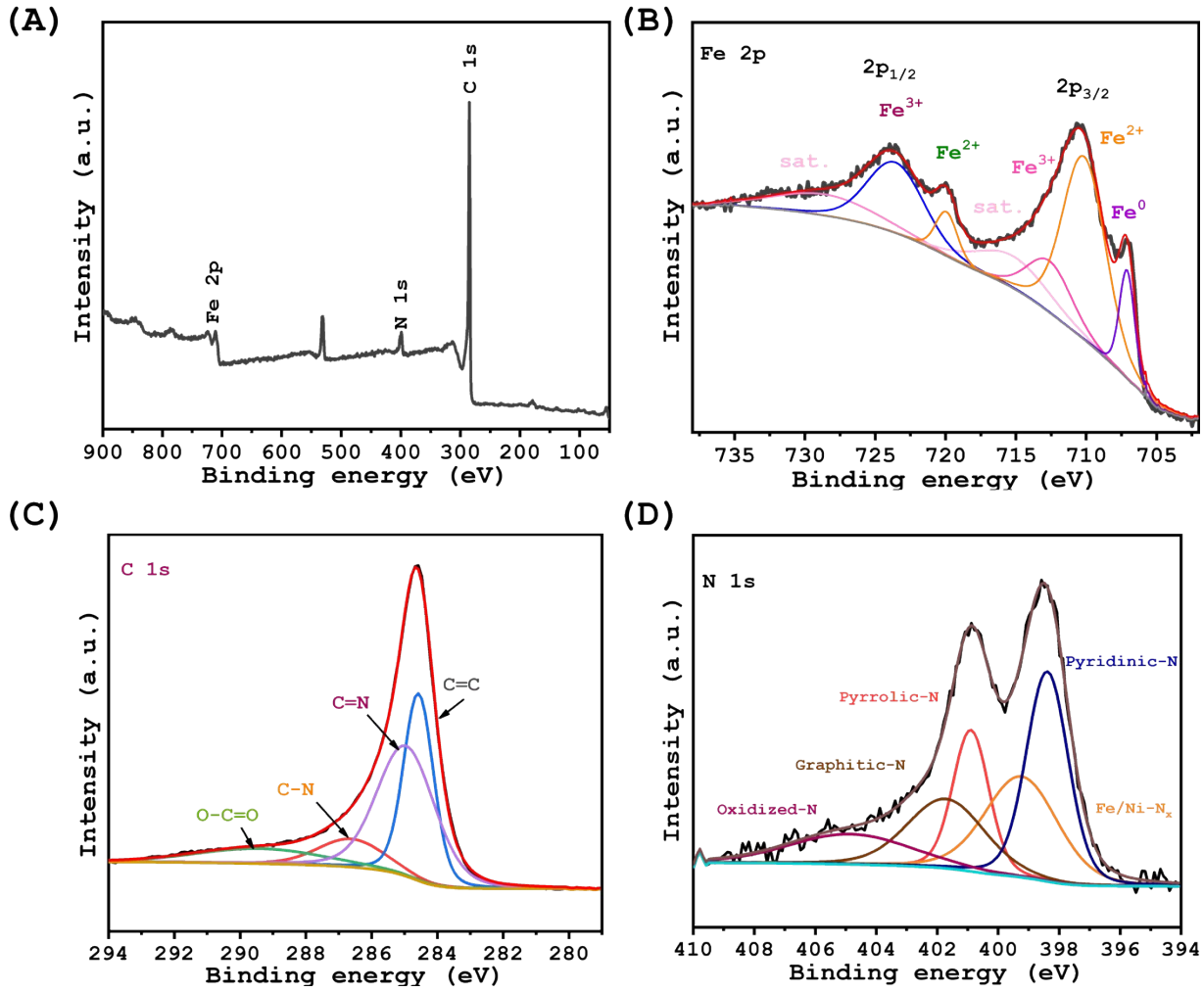

155

156 Figure **S6**. XPS studies for Fe-N-CM-KCC, (A) survey spectrum, (B) Fe 2p, (C) C 1s, and (D) N

157 1s.

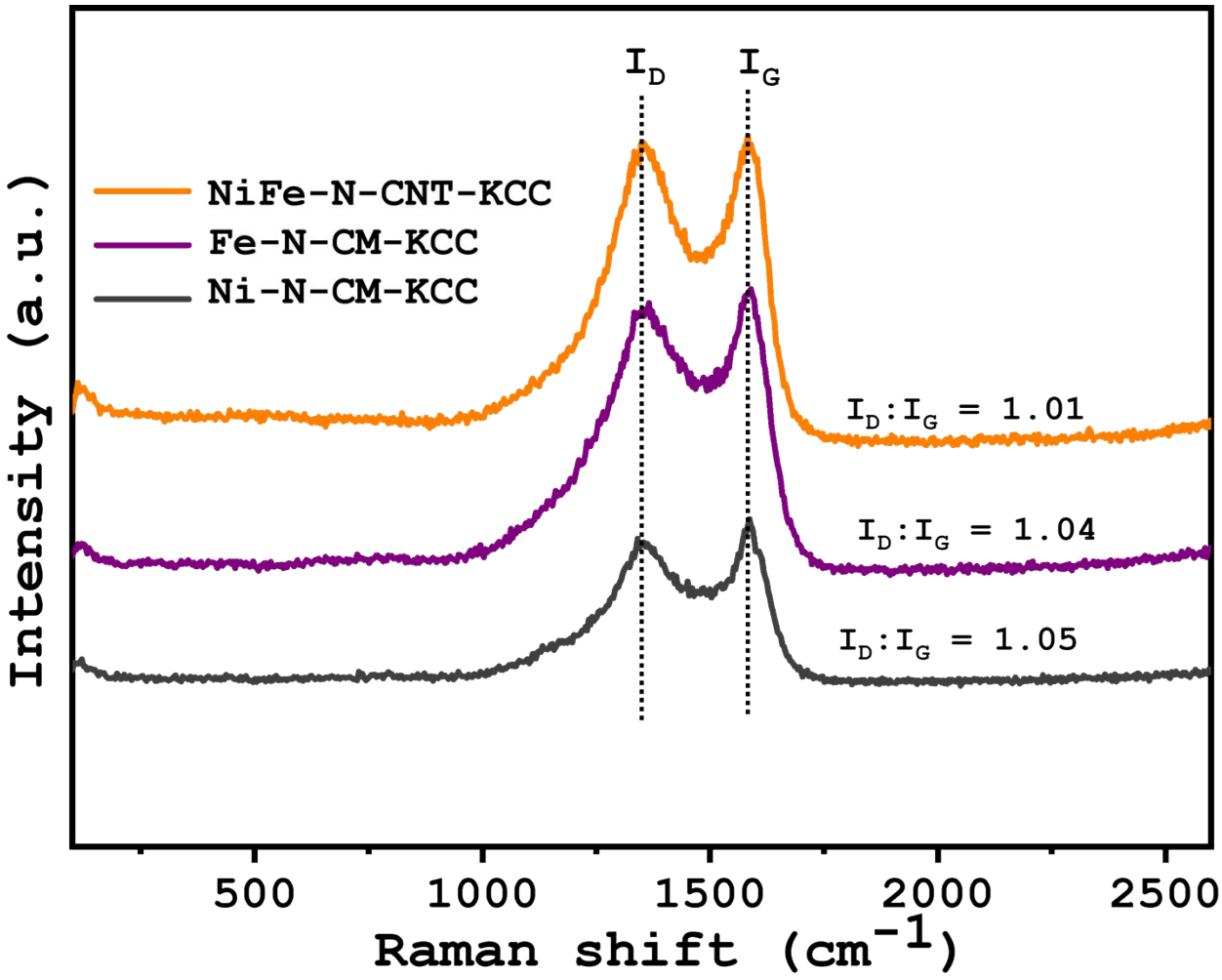

158

159 Figure S7. Raman spectra for Ni-N-CM-KCC, Fe-N-CM-KCC, and NiFe-N-CNT-KCC.

160

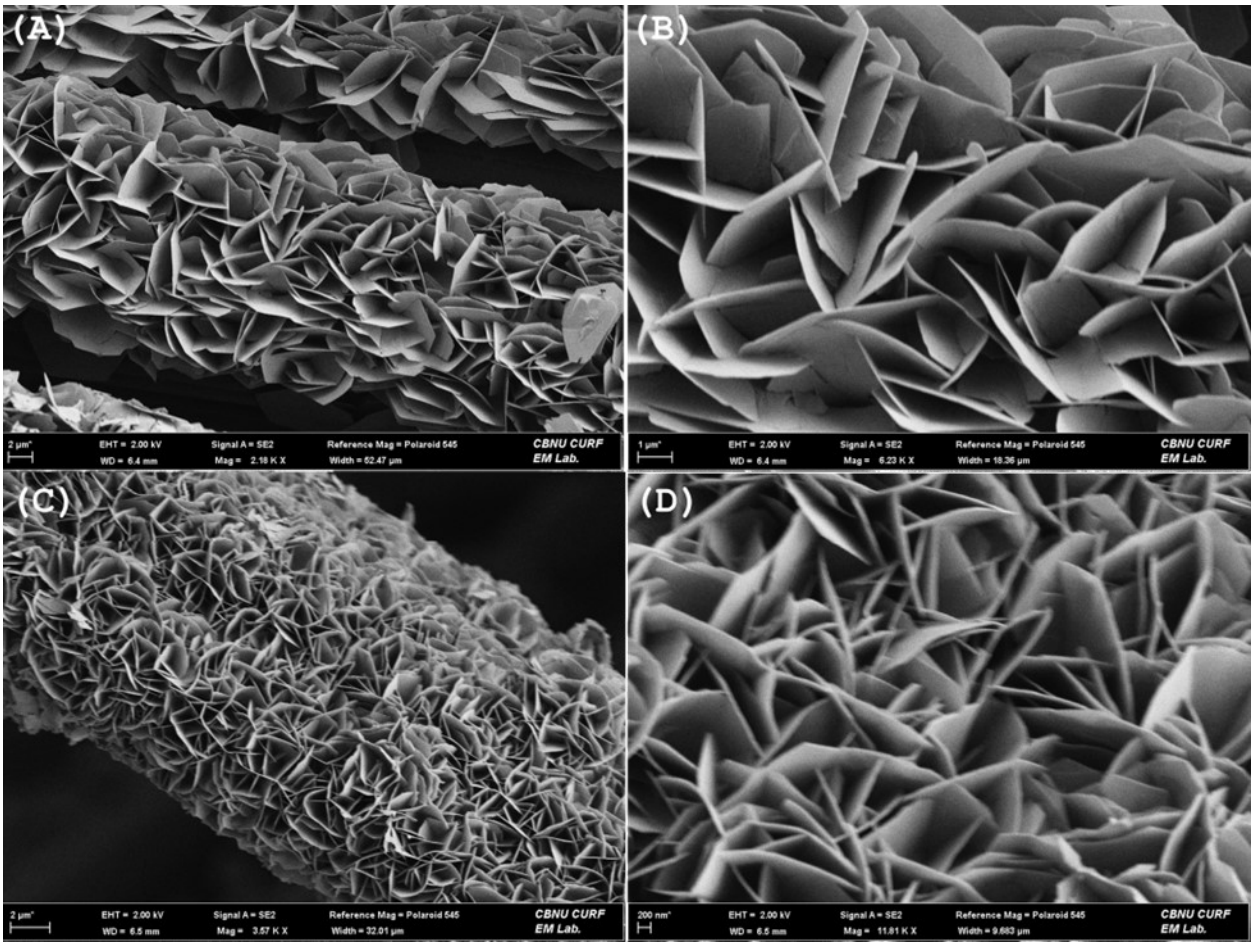

Figure S8. FESEM image of (A-B) Ni-$(OH)_2$ and (C-D) Ni-MOF at different magnifications.

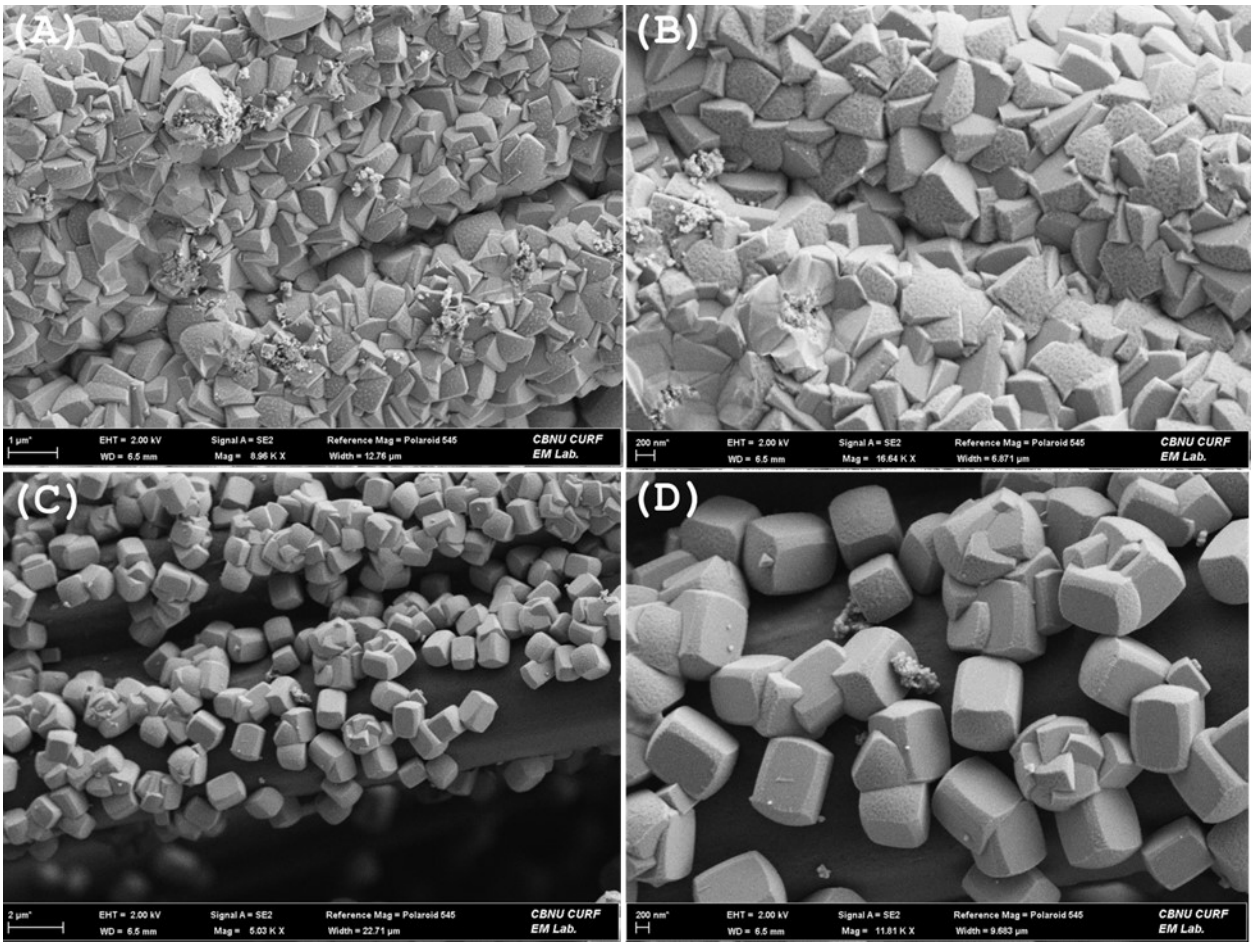

164

165 Figure S9. FESEM image of (A-B) FeO(OH) and (C-D) Fe-MOF at different magnifications.

166

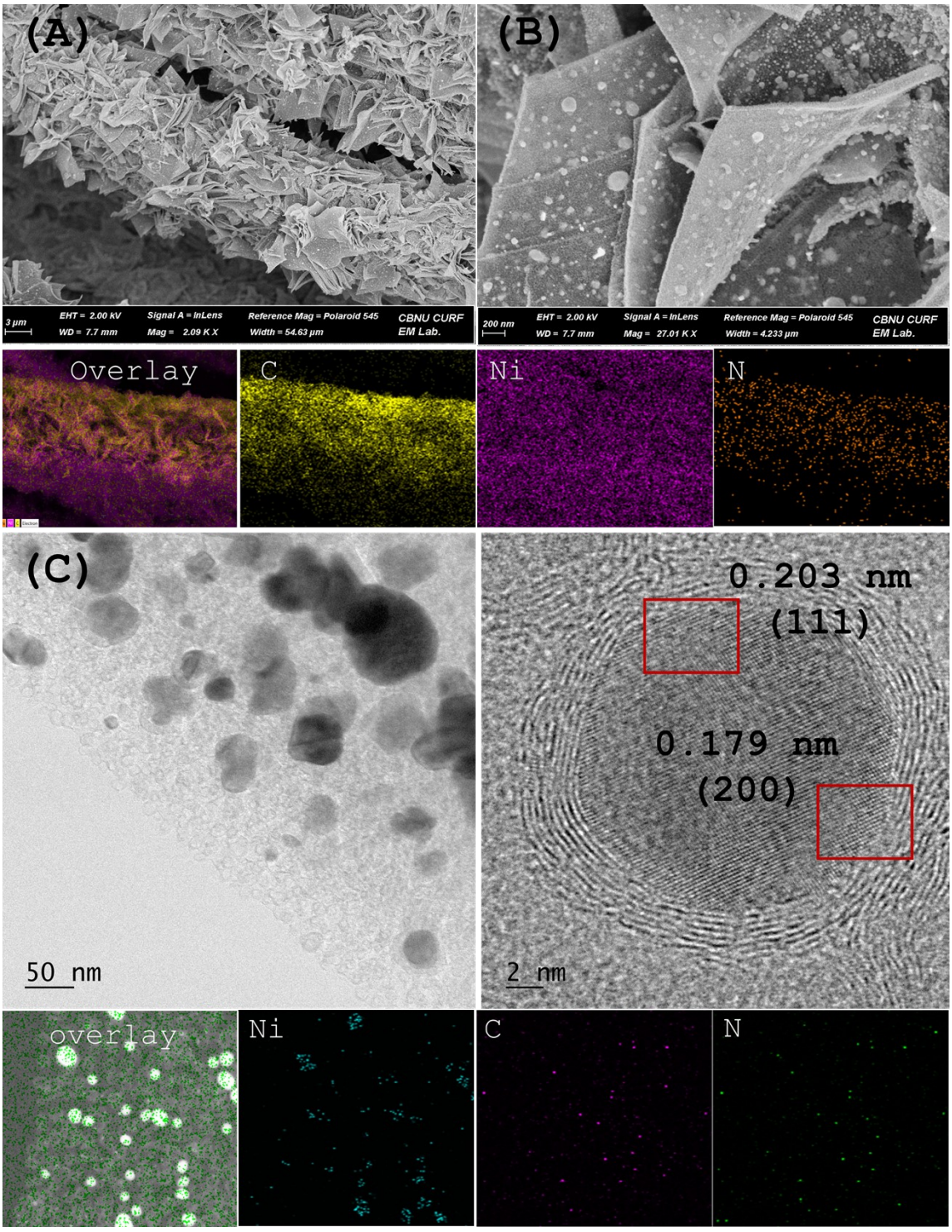

Figure **S10**. Morphological and microstructure studies for Ni-N-CM-KCC, (A, and B) FESEM images of Ni-N-CM-CC, (C, and D) TEM and HRTEM images of Ni-N-CM-KCC at different magnifications and corresponding EDS mapping.

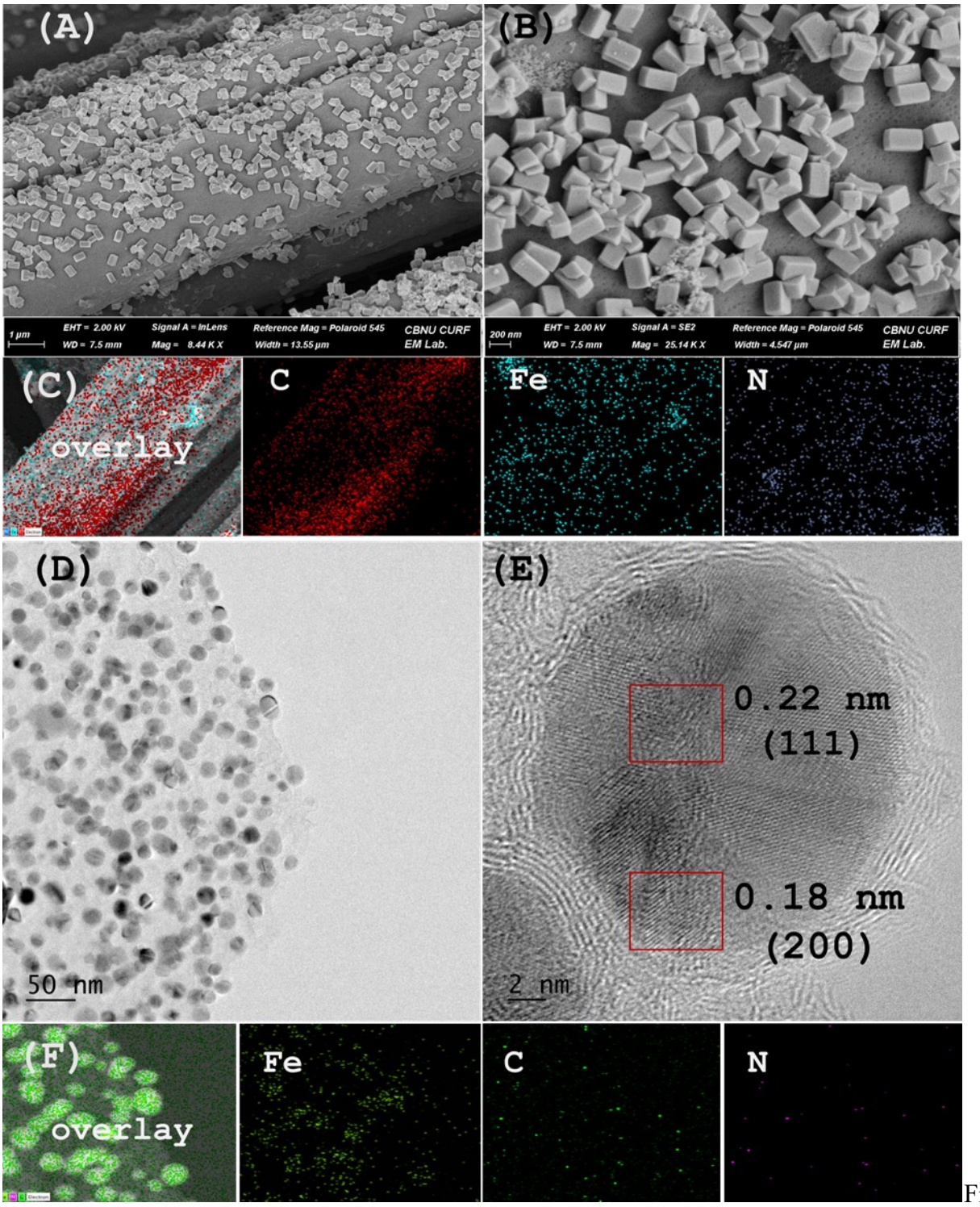

Figure **S11.** Morphological and microstructure studies for Fe-N-CM-KCC, (A, and B) FESEM images of Fe-N-CM-KCC, (C, and D) TEM and HRTEM images of Fe-N-CM-KCC at different magnifications and corresponding EDS mapping.

175

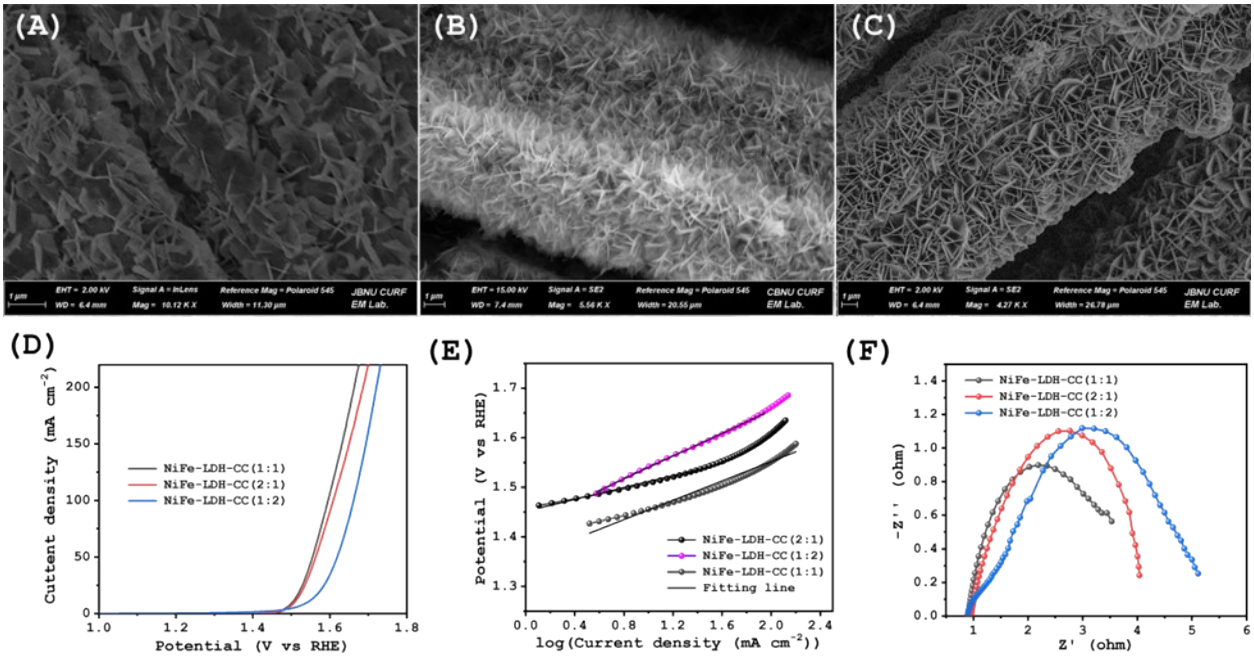

176

177 Figure S12: Morphology and electrochemical studies of optimized samples (NiFe-LDH at

178 different Ni:Fe ratio).

179

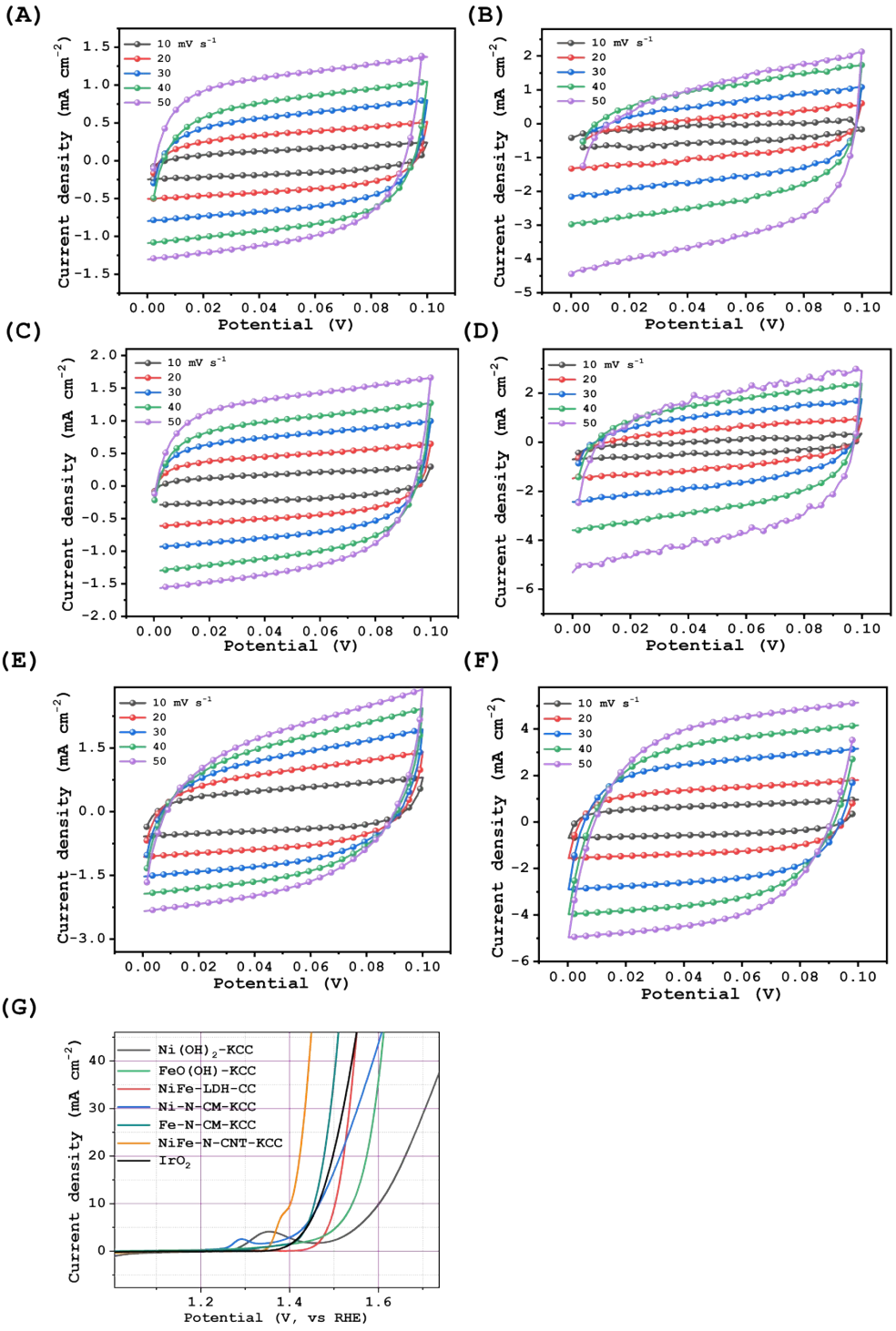

180

181 Figure **S13.** Cyclic voltammogram profiles of $Ni(OH)_2$-KCC, (B) Ni-N-CM-KCC, (C) FeO(OH)

182 -KCC, (D) Fe-N-CM-KCC, (E) NiFe-LDH-KCC, and (F) NiFe-N-CNT-KCC in the non-faradaic

183 region at various scan rates, (G) LSV profiles indicating the respective oxidation peaks.

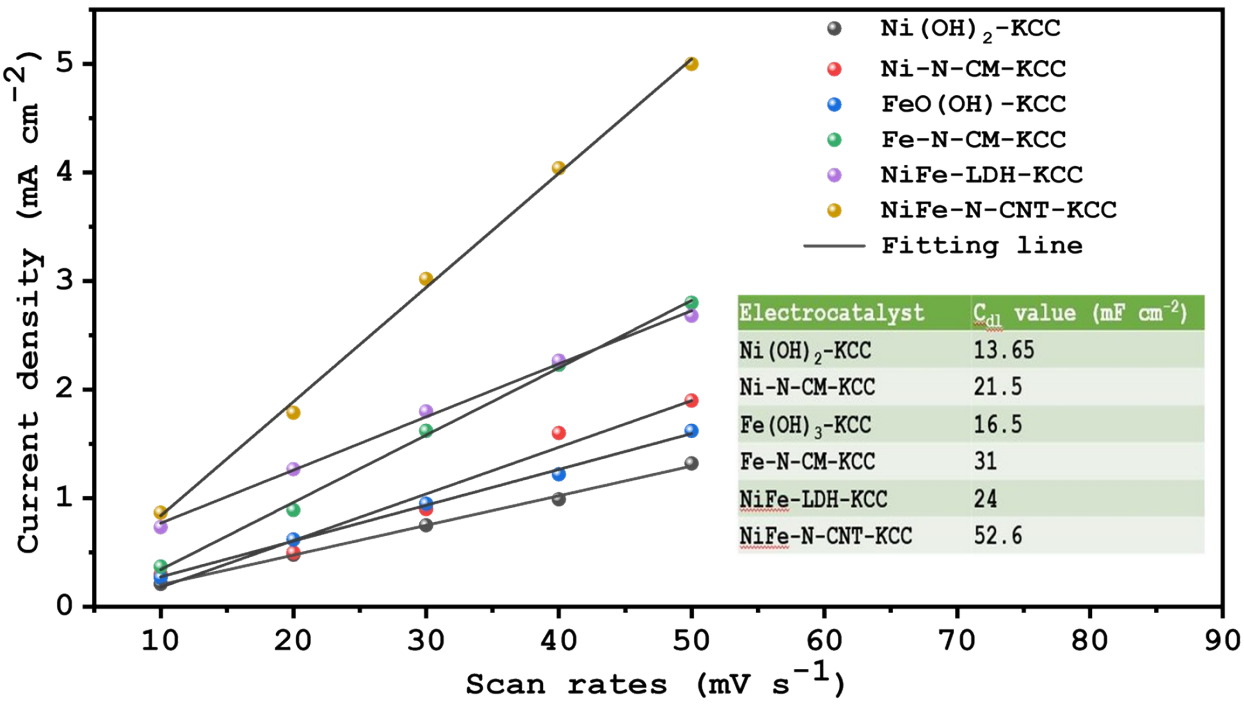

Electrocatalyst	C_{dl} value (mF cm^{-2})
Ni(OH)$_2$-KCC	13.65
Ni-N-CM-KCC	21.5
Fe(OH)$_3$-KCC	16.5
Fe-N-CM-KCC	31
NiFe-LDH-KCC	24
NiFe-N-CNT-KCC	52.6

184

185 Figure **S14**. Current density plotted against scan rates for all electrocatalyst (Inset; corresponding

186 C_{dl} values for all electrocatalysts).

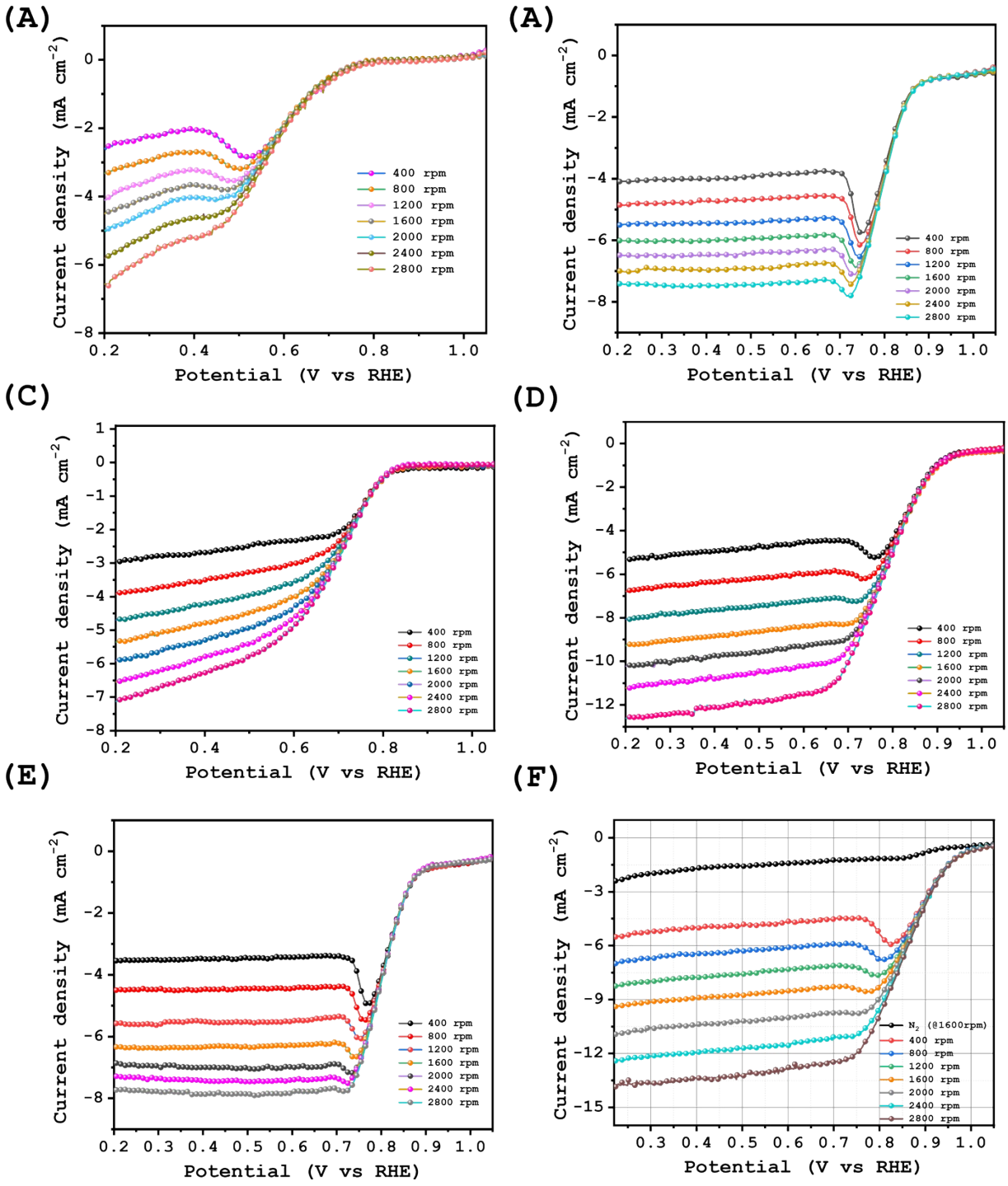

187

188 Figure **S15.** Linear sweep voltammogram (LSV) curves for $Ni(OH)_2$-KCC, (B) Ni-N-CM-KCC,

189 (C) FeO(OH) -KCC, (D) Fe-N-CM-KCC, (E) NiFe-LDH-KCC, and (F) NiFe-N-CNT-KCC

190 catalysts at different rotating speeds under continuous O_2 flow electrolytes.

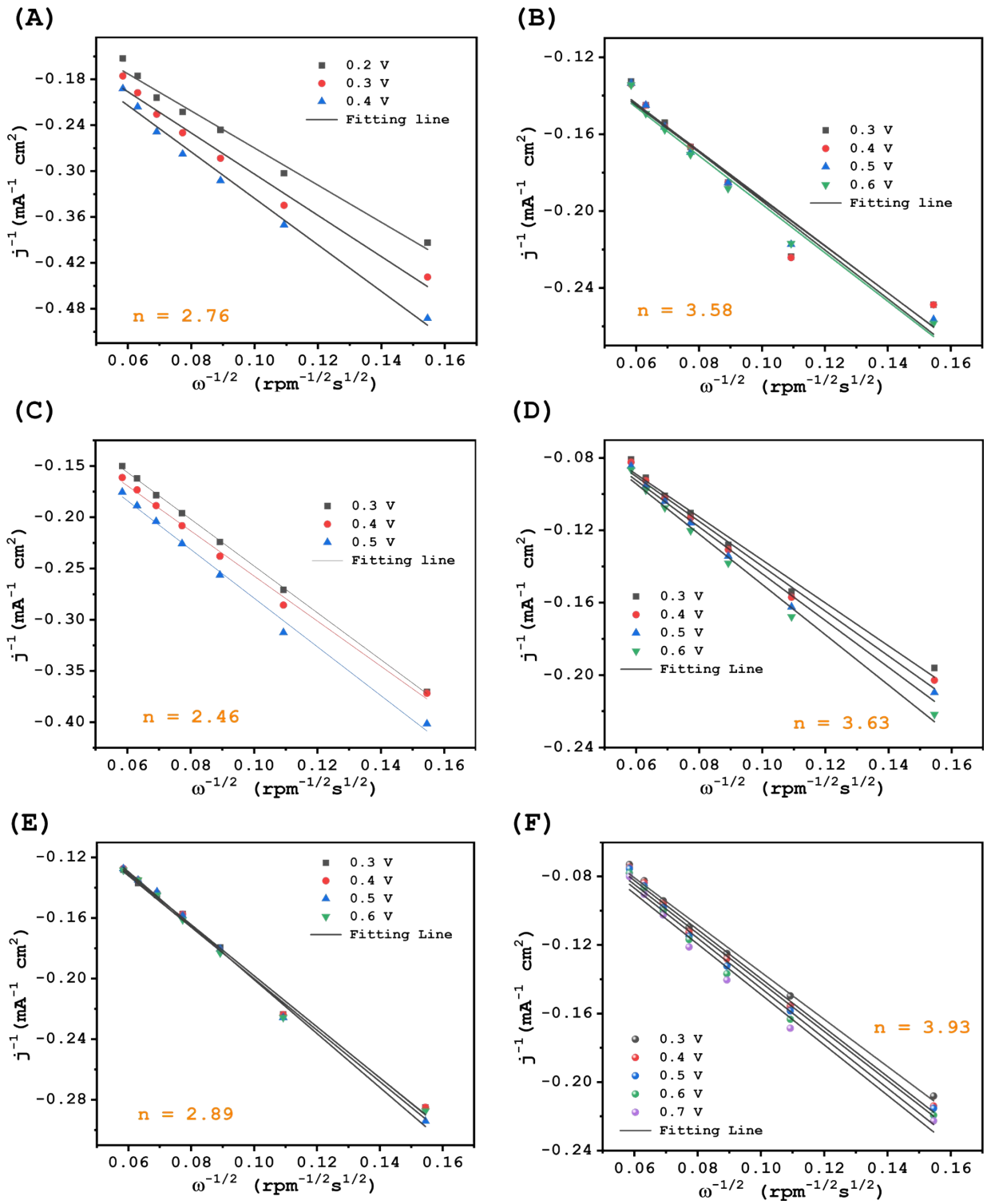

191

192 Figure **S16.** K-L plots for (a) $Ni(OH)_2$-KCC, (b) Ni-N-CM-KCC, (c) FeO(OH)-KCC, (D) Fe-N-

193 CM-KCC, (E) NiFe-LDH-KCC, and (F) NiFe-N-CNT-KCC at various potentials.

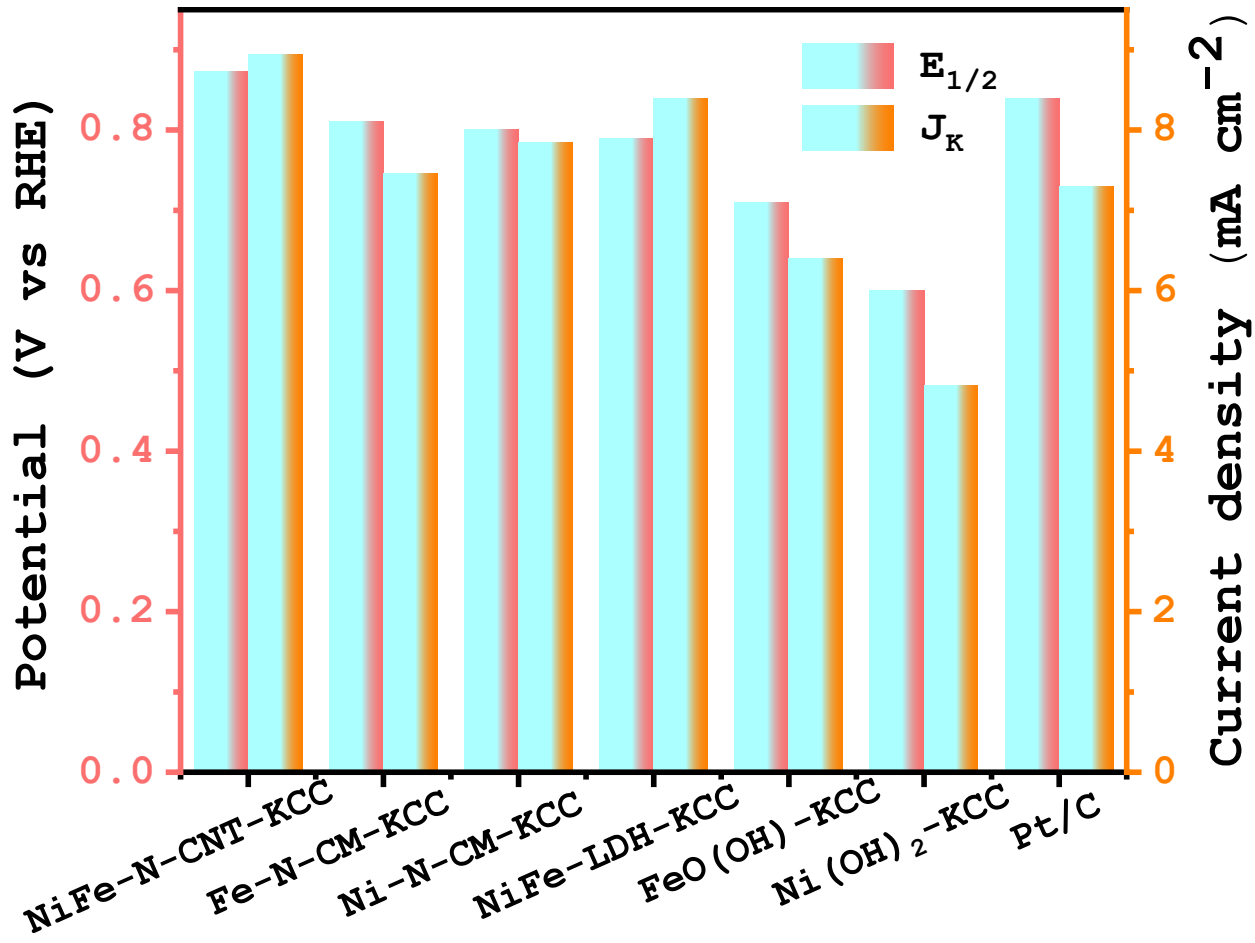

194

195 Figure S17. Summary of halfwave potential and kinetic current density for all samples at

196 respective potential

197

198

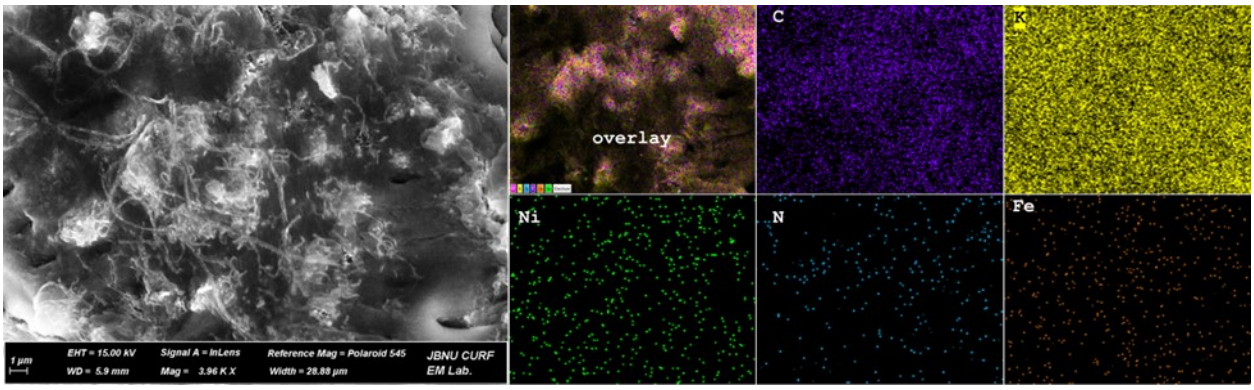

Figure S18: FESEM image and corresponding EDS mapping for NiFe-N-CNT-KCC after long term OER stability.

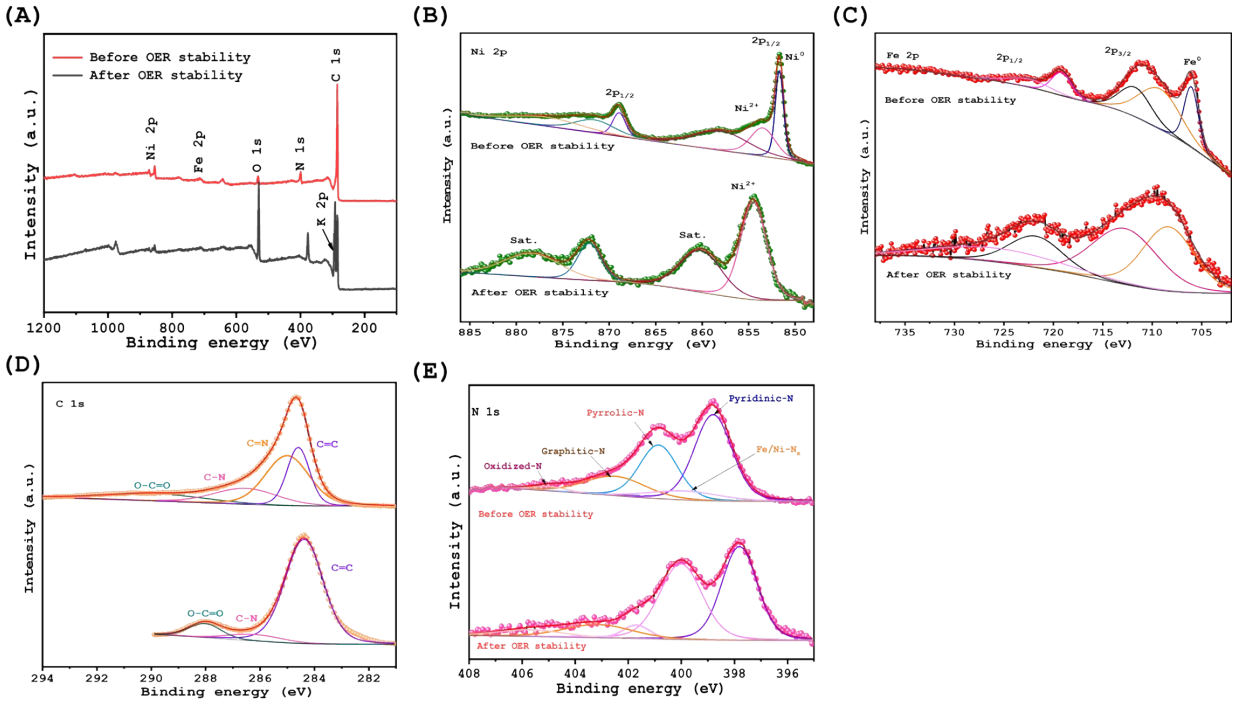

202

203 Figure S19: XPS studies for NiFe-N-CNT-KCC after long term OER stability, (A) XPS survey
204 spectrum indicating the presence of Ni, Fe, N, C, K and O elements, (B) Ni 2p, (C) Fe 2p, (D) C
205 1s, and (E) N 1s HR-XPS spectrum. After long term OER activity, the coordination status of Ni,
206 Fe, C as well O present distinct variation, as a result of formation of oxides or oxyhydroxides. The
207 extensive presence of pyridinic-N can be observed. The electron accepting pyridinic-N group can
208 impart the relatively high positive charge to the adjacent sp^2-bonded C atoms, thus facilitating
209 electron transfer between catalyst surface and reaction intermediates.

210 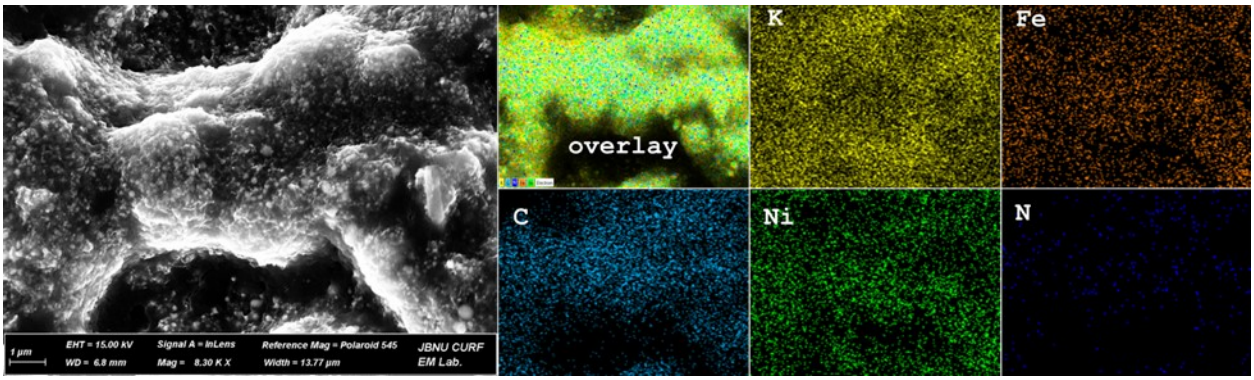

211 Figure S20: FESEM image and corresponding EDS mapping for NiFe-N-CNT-KCC after long

212 term ORR stability.

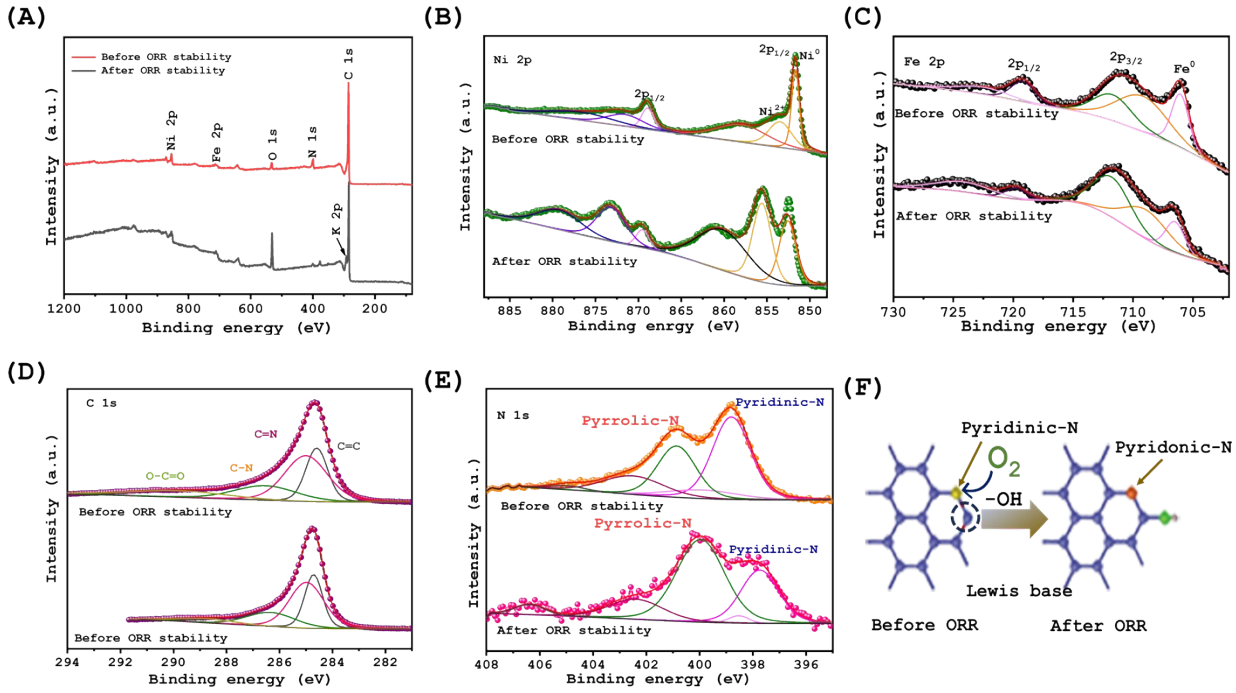

Figure S21: XPS studies for NiFe-N-CNT-CC after long term ORR stability, (A) XPS survey spectrum indicating the presence of Ni, Fe, N, C, K and O elements, (B) Ni 2p, (C) Fe 2p, (D) C 1s, (E) N 1s HR-XPS spectrum, and schematic illustration of transformation of pyridinic-N to pyridonic-N. HR-XPS of Ni 2p and Co 2p almost retain its originality with the signature metallic peaks, implying the well encapsulation of alloy nanoparticles by carbon shells . An obvious change in N peaks after ORR can be identified. Pyridinic-N content in NiFe-N-CNT-KCC after ORR can be decreased indicating the transformation to pyridonic-N. such kind of transformation is beneficial to the improvement of the overall ORR.

225 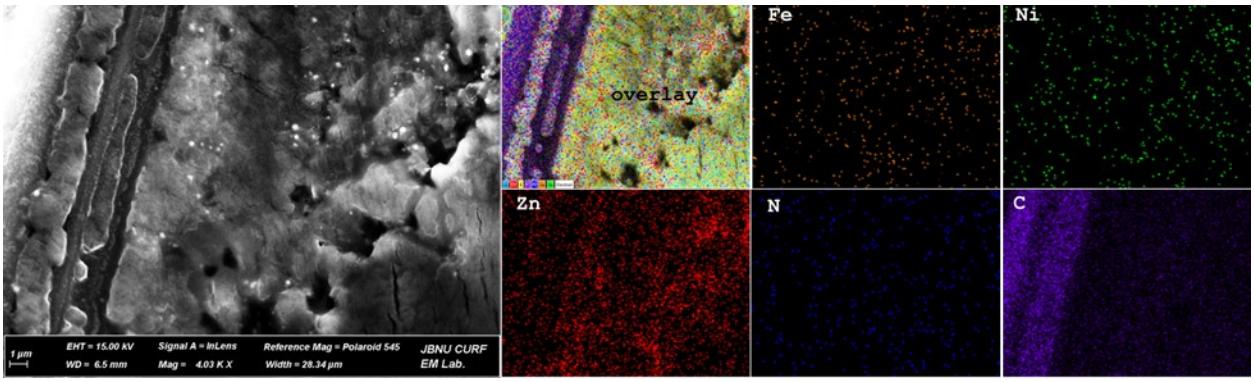

226 Figure S21: FESEM image and corresponding EDS mapping for NiFe-N-CNT-KCC after long

227 term NiFe-N-CNT-KCC based aqueous Zn air battery stability.

228

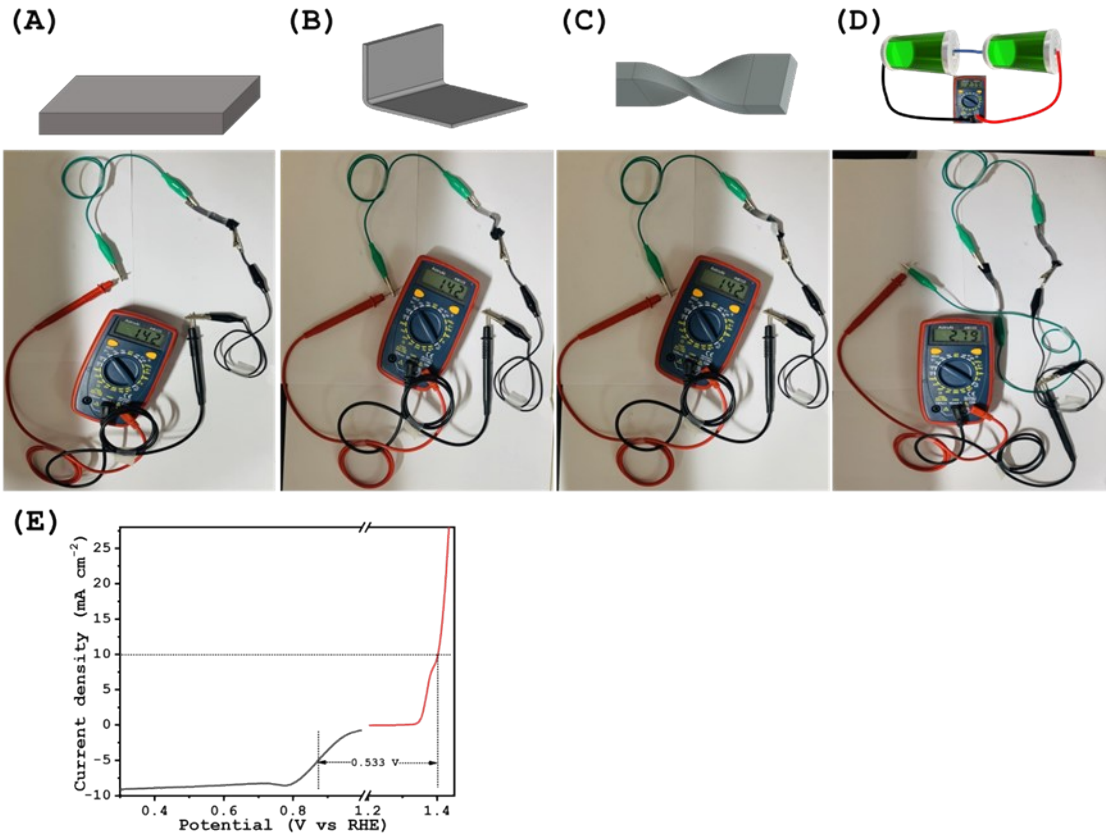

229

230 Figure S22. (A, B and C) NiFe-N-CNT-KCC based solid flexible zinc air battery performance at
231 different orientation with their schematic representations, (D) power output when two NiFe-N-
232 CNT-KCC based solid flexible zinc air batteries connected in series delivered ~2.8 V, and (E)
233 ORR and OER LSV curves of the NiFe-N-CNT-KCC at 0.1 M KOH electrolyte conditions and
234 its cell potential difference indicating the reversibility.

Table ST1. Comparison of OER activity for NiFe-N-CNT-KCC with previously reported catalysts in 1 M KOH

S.N.	Electrocatalysts	Overpotential (@10 mA cm^{-2})	Tafel slope ($mV\ dec^{-1}$)	Ref.
1.	FeNi@N-CNT	300	47.7	[3]
2.	sAu/NiFe LDH	237	36	[4]
3.	Co/N@CNTs@CNMF-800	310	61.3	[5]
4.	Fe SAs/NC	320	55.5	[6]
5.	VMoON@NC	187	19.4	[7]
6.	NPCNF-O	326	178	[8]
7.	^{SA}Ru/NiFe LDH	251	98.1	[9]
8.	Gelled FeCoW	191	37	[10]
9.	NixFe1-xSe2-DO	195	28	[11]
10.	Fe0.09Co0.13-NiSe2	251	63	[12]
11.	FeNi/N-CPCF-950	355	67	[13]
12.	FeNiP/NPCS	318	95	[14]
13.	CoNi/BCF	370	166	[15]
14.	FeNi-NC	380	115	[16]
15.	Co_2Fe_1@NC	420	141	[17]
16.	Mn-RuO_2	270	45.8	[18]
17.	NiFe-N-CNT-KCC	173	37.87	This work

Table ST2. Comparison of ORR activity for NiFe-N-CNT-KCC with previously reported catalysts in 0.1 M KOH

S.N.	Electrocatalysts	Half wave potential (v)	Tafel value (mV dec^{-1})	Ref.
1.	Co@NCNTA-700	0.861	97	[19]
2.	Co/N@CNTs@CNMF-800	0.86	61.3	[5]
3.	Fe SAs/NC	0.83	66.2	[6]
4.	VMoON@NC	0.861	26.6	[7]
5.	Fe-NC	0.842	47	[20]
6.	NPCNF-0	0.85	86	[8]
7.	FeNi/N-CPCF-950	0.864	66	[13]
8.	FeNiP/NPCS	0.84	91	[14]
9.	CoNi/BCF	0.80	44	[15]
10.	FeNi-NC	0.83	-	[16]
11.	Co_2Fe_1@NC	0.85	66.2	[17]
12.	Mn-RuO2	0.86	38.9	[18]
13.	NiFe-N-CNT-KCC	0.87	25.74	This work

Table ST3. Comparison of Zn-air battery performance

S.N.	Electrocatalysts	Current density (mA cm^{-2})	OCV (V)	Sp. Capacitance (mA h g^{-1})	Stability	Power density (mW cm^{-2})	Ref.
1.	NCNT/MnO-$(MnFe)_2O_3$	160	1.45	647	2.2 h	98	[21]
2.	NCNT/CoFe-$CoFe_2O_4$	160	1.56	727	202 h	98	[21]
3.	FeCo-NCNFs-800		1.48	-	125	74	[22]
4.	Co/MnO@NC	250	1.50	768	335	146	[23]
5.	$Fe_{1.2}(CoNi)_{1.8}S_6$ MES	270	1.45	808	420 cycles/140 h	124	[24]
6.	CoNi@NCNTs/CC	221	1.49	782	370	80	[25]
7.	FeCoMoS@NG	230	1.44	789	72 h	118	[26]
8.	Fe-N-C/N-OMC	180	1.55	711	66 h	113	[27]
9.	SA-PtCoF	266	1.50	808	240 h	125	[28]
10	$CaCu_3Ti_4O_{12}$ (CCTO)					127	
11	$Co_{1-x}SnO_{3-y}$-$Fe_{0.021}$A/C		1.37	-	60 min	50	[29]
12	H-NiFe/CNF		1.23	-	120 cycles	85.3	[30]
13	NiFe-N-CNT-KCC	282	1.55	831	140 h	153.03	This work

Reference:

[1] Y. Zhou, R. Lu, X. Tao, Z. Qiu, G. Chen, J. Yang, Y. Zhao, X. Feng, K. Müllen, Boosting Oxygen Electrocatalytic Activity of Fe–N–C Catalysts by Phosphorus Incorporation, Journal of the American Chemical Society, 145 (2023) 3647-3655.

[2] Y. Li, J. Gao, F. Zhang, Q. Qian, Y. Liu, G. Zhang, Hierarchical 3D macrosheets composed of interconnected in situ cobalt catalyzed nitrogen doped carbon nanotubes as superior bifunctional oxygen electrocatalysts for rechargeable Zn–air batteries, Journal of Materials Chemistry A, 6 (2018) 15523-15529.

[3] Z. Tao, T. Wang, X. Wang, J. Zheng, X. Li, MOF-Derived Noble Metal Free Catalysts for Electrochemical Water Splitting, ACS Applied Materials & Interfaces, 8 (2016) 35390-35397.

[4] J. Zhang, J. Liu, L. Xi, Y. Yu, N. Chen, S. Sun, W. Wang, K.M. Lange, B. Zhang, Single-Atom Au/NiFe Layered Double Hydroxide Electrocatalyst: Probing the Origin of Activity for Oxygen Evolution Reaction, Journal of the American Chemical Society, 140 (2018) 3876-3879.

[5] T. Liu, J. Mou, Z. Wu, C. Lv, J. Huang, M. Liu, A Facile and Scalable Strategy for Fabrication of Superior Bifunctional Freestanding Air Electrodes for Flexible Zinc–Air Batteries, Advanced Functional Materials, 30 (2020) 2003407.

[6] Z. Li, S. Ji, C. Xu, L. Leng, H. Liu, J.H. Horton, L. Du, J. Gao, C. He, X. Qi, Q. Xu, J. Zhu, Engineering the Electronic Structure of Single-Atom Iron Sites with Boosted Oxygen Bifunctional Activity for Zinc–Air Batteries, Advanced Materials, 35 (2023) 2209644.

[7] J. Balamurugan, P.M. Austeria, J.B. Kim, E.-S. Jeong, H.-H. Huang, D.H. Kim, N. Koratkar, S.O. Kim, Electrocatalysts for Zinc-air Batteries Featuring Single Molybdenum Atoms in a Nitrogen-doped Carbon Framework, Advanced Materials, n/a (2023) 2302625.

[8] F. Qiang, J. Feng, H. Wang, J. Yu, J. Shi, M. Huang, Z. Shi, S. Liu, P. Li, L. Dong, Oxygen Engineering Enables N-Doped Porous Carbon Nanofibers as Oxygen Reduction/Evolution Reaction Electrocatalysts for Flexible Zinc–Air Batteries, ACS Catalysis, 12 (2022) 4002-4015.

[9] Y. Yang, Q.-N. Yang, Y.-B. Yang, P.-F. Guo, W.-X. Feng, Y. Jia, K. Wang, W.-T. Wang, Z.-H. He, Z.-T. Liu, Enhancing Water Oxidation of Ru Single Atoms via Oxygen-Coordination Bonding with NiFe Layered Double Hydroxide, ACS Catalysis, 13 (2023) 2771-2779.

[10] B. Zhang, X. Zheng, O. Voznyy, R. Comin, M. Bajdich, M. García-Melchor, L. Han, J. Xu, M. Liu, L. Zheng, F.P. García de Arquer, C.T. Dinh, F. Fan, M. Yuan, E. Yassitepe, N. Chen, T. Regier, P. Liu, Y. Li, P. De Luna, A. Janmohamed, H.L. Xin, H. Yang, A. Vojvodic, E.H. Sargent, Homogeneously dispersed multimetal oxygen-evolving catalysts, Science, 352 (2016) 333-337.

[11] X. Xu, F. Song, X. Hu, A nickel iron diselenide-derived efficient oxygen-evolution catalyst, Nature Communications, 7 (2016) 12324.

[12] Y. Sun, K. Xu, Z. Wei, H. Li, T. Zhang, X. Li, W. Cai, J. Ma, H.J. Fan, Y. Li, Strong Electronic Interaction in Dual-Cation-Incorporated NiSe2 Nanosheets with Lattice Distortion for Highly Efficient Overall Water Splitting, Advanced Materials, 30 (2018) 1802121.

[13] Z. Wang, J. Ang, J. Liu, X.Y.D. Ma, J. Kong, Y. Zhang, T. Yan, X. Lu, FeNi alloys encapsulated in N-doped CNTs-tangled porous carbon fibers as highly efficient and durable bifunctional oxygen electrocatalyst for rechargeable zinc-air battery, Applied Catalysis B: Environmental, 263 (2020) 118344.

[14] J.-T. Ren, Y.-S. Wang, L. Chen, L.-J. Gao, W.-W. Tian, Z.-Y. Yuan, Binary FeNi phosphides dispersed on N,P-doped carbon nanosheets for highly efficient overall water splitting and rechargeable Zn-air batteries, Chemical Engineering Journal, 389 (2020) 124408.

[15] W. Wan, X. Liu, H. Li, X. Peng, D. Xi, J. Luo, 3D carbon framework-supported CoNi nanoparticles as bifunctional oxygen electrocatalyst for rechargeable Zn-air batteries, Applied Catalysis B: Environmental, 240 (2019) 193-200.
[16] L. Yang, X. Zeng, D. Wang, D. Cao, Biomass-derived FeNi alloy and nitrogen-codoped porous carbons as highly efficient oxygen reduction and evolution bifunctional electrocatalysts for rechargeable Zn-air battery, Energy Storage Materials, 12 (2018) 277-283.
[17] T. Tang, W.-J. Jiang, X.-Z. Liu, J. Deng, S. Niu, B. Wang, S.-F. Jin, Q. Zhang, L. Gu, J.-S. Hu, L.-J. Wan, Metastable Rock Salt Oxide-Mediated Synthesis of High-Density Dual-Protected M@NC for Long-Life Rechargeable Zinc–Air Batteries with Record Power Density, Journal of the American Chemical Society, 142 (2020) 7116-7127.
[18] C. Zhou, X. Chen, S. Liu, Y. Han, H. Meng, Q. Jiang, S. Zhao, F. Wei, J. Sun, T. Tan, R. Zhang, Superdurable Bifunctional Oxygen Electrocatalyst for High-Performance Zinc–Air Batteries, Journal of the American Chemical Society, 144 (2022) 2694-2704.
[19] L. Liu, Y. Wang, F. Yan, C. Zhu, B. Geng, Y. Chen, S.-l. Chou, Cobalt-Encapsulated Nitrogen-Doped Carbon Nanotube Arrays for Flexible Zinc–Air Batteries, Small Methods, 4 (2020) 1900571.
[20] J. Roh, A. Cho, S. Kim, K.-S. Lee, J. Shin, J.S. Choi, J. Bak, S. Lee, D. Song, E.-J. Kim, C. Lee, Y.R. Uhm, Y.-H. Cho, J.W. Han, E. Cho, Transformation of the Active Moiety in Phosphorus-Doped Fe–N–C for Highly Efficient Oxygen Reduction Reaction, ACS Catalysis, (2023) 9427-9441.
[21] Q. Qin, P. Li, L. Chen, X. Liu, Coupling Bimetallic Oxides/Alloys and N-Doped Carbon Nanotubes as Tri-Functional Catalysts for Overall Water Splitting and Zinc–Air Batteries, ACS Applied Materials & Interfaces, 10 (2018) 39828-39838.
[22] L. Yang, S. Feng, G. Xu, B. Wei, L. Zhang, Electrospun MOF-Based FeCo Nanoparticles Embedded in Nitrogen-Doped Mesoporous Carbon Nanofibers as an Efficient Bifunctional Catalyst for Oxygen Reduction and Oxygen Evolution Reactions in Zinc-Air Batteries, ACS Sustainable Chemistry & Engineering, 7 (2019) 5462-5475.
[23] Y. Niu, X. Teng, S. Gong, X. Liu, M. Xu, Z. Chen, Boosting oxygen electrocatalysis for flexible zinc-air batteries by interfacing iron group metals and manganese oxide in porous carbon nanowires, Energy Storage Materials, 43 (2021) 42-52.
[24] H. Wu, Z. Li, Z. Wang, Y. Ma, S. Huang, F. Ding, F. Li, Q. Zhai, Y. Ren, X. Zheng, Y. Yang, S. Tang, Y. Deng, X. Meng, Regulation of electronic structure in medium-entropy metal sulfides nanoparticles as highly efficient bifunctional electrocatalysts for zinc-air battery, Applied Catalysis B: Environmental, 325 (2023) 122356.
[25] W.-W. Tian, J.-T. Ren, Z.-Y. Yuan, In-situ cobalt-nickel alloy catalyzed nitrogen-doped carbon nanotube arrays as superior freestanding air electrodes for flexible zinc-air and aluminum-air batteries, Applied Catalysis B: Environmental, 317 (2022) 121764.
[26] S. Ramakrishnan, J. Balamurugan, M. Vinothkannan, A.R. Kim, S. Sengodan, D.J. Yoo, Nitrogen-doped graphene encapsulated FeCoMoS nanoparticles as advanced trifunctional catalyst for water splitting devices and zinc–air batteries, Applied Catalysis B: Environmental, 279 (2020) 119381.
[27] J. Han, H. Bao, J.-Q. Wang, L. Zheng, S. Sun, Z.L. Wang, C. Sun, 3D N-doped ordered mesoporous carbon supported single-atom Fe-N-C catalysts with superior performance for oxygen reduction reaction and zinc-air battery, Applied Catalysis B: Environmental, 280 (2021) 119411.
[28] Z. Li, W. Niu, Z. Yang, N. Zaman, W. Samarakoon, M. Wang, A. Kara, M. Lucero, M.V. Vyas, H. Cao, H. Zhou, G.E. Sterbinsky, Z. Feng, Y. Du, Y. Yang, Stabilizing atomic Pt with trapped interstitial F in alloyed PtCo nanosheets for high-performance zinc-air batteries, Energy & Environmental Science, 13 (2020) 884-895.
[29] C. Ye, H. Cheng, L. Zheng, J. Lin, Q. Xu, Y. Qiu, Z. Pan, Y. Qiu, Tailoring Metal–Oxygen Bonds Boosts Oxygen Reaction Kinetics for High-Performance Zinc–Air Batteries, Nano Letters, 23 (2023) 1573-1581.

[30] H. Lei, L. Ma, Q. Wan, Z. Huangfu, S. Tan, Z. Wang, W. Mai, Porous carbon nanofibers confined NiFe alloy nanoparticles as efficient bifunctional electrocatalysts for Zn-air batteries, Nano Energy, 104 (2022) 107941.